

Paper contributed to the X International Symposium on Lepton and Photon Interactions at High Energies, 23rd-28th July 2001, Rome, Italy.

Results and plans of the CRESST dark matter search

M. Altmann^b, G. Angloher^d, M. Bruckmayer^b, C. Bucci^a, S. Cooper^d,
C. Cozzini^b, P. DiStefano^b, F. von Feilitzsch^c, T. Frank^b, D. Hauff^b,
Th. Jagemann^c, J. Jochum^c, R. Keeling^d, H. Kraus^d, J. Macallister^d,
F. Pröbst^{b,2}, Y. Ramachers^d, J. Schnagl^c, W. Seidel^b, I. Sergeev^{b,1}, M. Stark^c,
L. Stodolsky^b, H. Wulandari^c

^a *Laboratori Nazionali del Gran Sasso, I-67010 Assergi, Italy*

^b *Max-Planck-Institut für Physik, Föhringer Ring 6, D-80805 Munich, Germany*

^c *Technische Universität München, Physik Department, D-85747 Munich, Germany*

^d *University of Oxford, Physics Department, Oxford OX1 3RH, U.K.*

Abstract

Data taken by CRESST in 2000 with a cryogenic detector system based on 262 g sapphire crystals is used to place limits on WIMP dark matter in the Galactic Halo. The detector is especially sensitive for low-mass WIMPS with spin-dependent cross sections and improves on existing limits in this region. CRESST is now preparing for a second phase, which will use a 10 kg detector consisting of 300 g CaWO₄ crystals with simultaneous detection of phonons and scintillation light to reduce background.

¹ *Permanent Address: Joint Institute for Nuclear Research, Dubna, 141980, Russia*

²Corresponding author; Tel.: +49 89 32354 270; E-mail: proebst@mppmu.mpg.de

The goal of the CRESST¹ experiment is to detect WIMP dark matter particles via the energy they deposit when elastically scattering on nuclei. We have developed very sensitive massive cryogenic detectors for this purpose and installed them in a low-background facility in the Gran Sasso Underground Laboratory (LNGS).

The first section of this paper describes our low-background facility in LNGS. The second section describes Phase I of the project, which used 262 g sapphire cryogenic calorimeters, and presents the resulting dark matter limits. The final section describes our plans for Phase II, using scintillating calorimeters to reduce the background.

1 Low-background facility

Since our detectors operate at ~ 15 mK, the central part of the CRESST low-background facility at the LNGS is the cryostat. The design of this cryostat had to combine the requirements of low temperatures with those of low background. The first-generation cryostats in this field were conventional dilution refrigerators where some of the materials were screened for radioactivity. However, due to cryogenic requirements some non-radiopure materials, for example stainless steel, cannot be completely avoided. Therefore we chose the design shown in Fig. 1, in which a well separated “cold box” houses the experimental volume at some distance from the dilution refrigerator. The experimental volume can house up to 100 kg of target mass. The cold box is made of low-background copper, with high-purity lead used for the vacuum seals. It is surrounded by shielding consisting of 14 cm of low-background copper and 20 cm of lead. Special consideration was given to the space between the dilution refrigerator and the cold box. The separation was chosen large enough so that the “neck” of the external shielding, together with the internal shields, eliminates any direct line of sight from the outside world into the cold box. The low temperature of the dilution refrigerator is transferred to the cold box by a 1.5 meter long cold finger protected by thermal radiation shields, all of low-background copper. A 20 cm thick lead shield inside a copper can is placed between the mixing chamber and the cold finger, with the low temperature transmitted here by the copper can. This internal shield, combined with another one surrounding the cold finger, serves to block any line of sight for radiation coming from the dilution refrigerator into the experimental volume.

To avoid activation of the copper by cosmic rays we minimized the amount of time that the copper of the shielding and the cold box spent above ground. After electrolytic production the copper was stored in the cellar of a beer brewery near Munich, shielded from cosmic rays by more than 10 m water equivalent. This reduces the hadronic component of the cosmic rays by a factor of about 500. Each piece was only brought out of the brewery cellar for the few days needed for its machining, and then returned to the cellar. The total above-ground exposure of the copper was about 10 weeks.

It is not sufficient to use high-purity materials. Their surfaces must also be kept clean during use, and we have taken care to design our facilities in Gran Sasso to make this possible. The Faraday cage which surrounds the experiment was chosen large enough so that all work

¹ Cryogenic Rare Event Search with Superconducting Thermometers

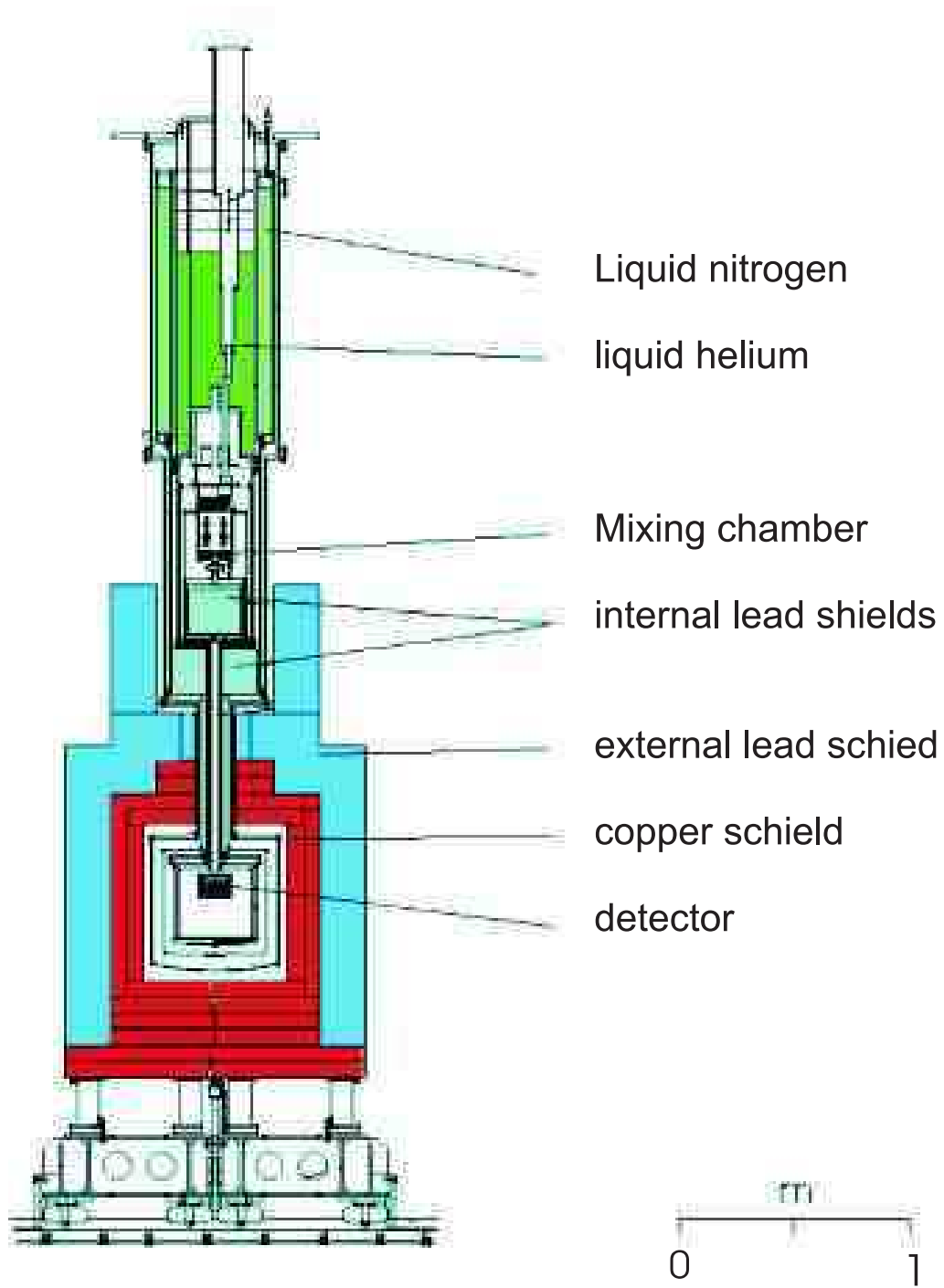


Figure 1: Layout of dilution refrigerator and cold box.

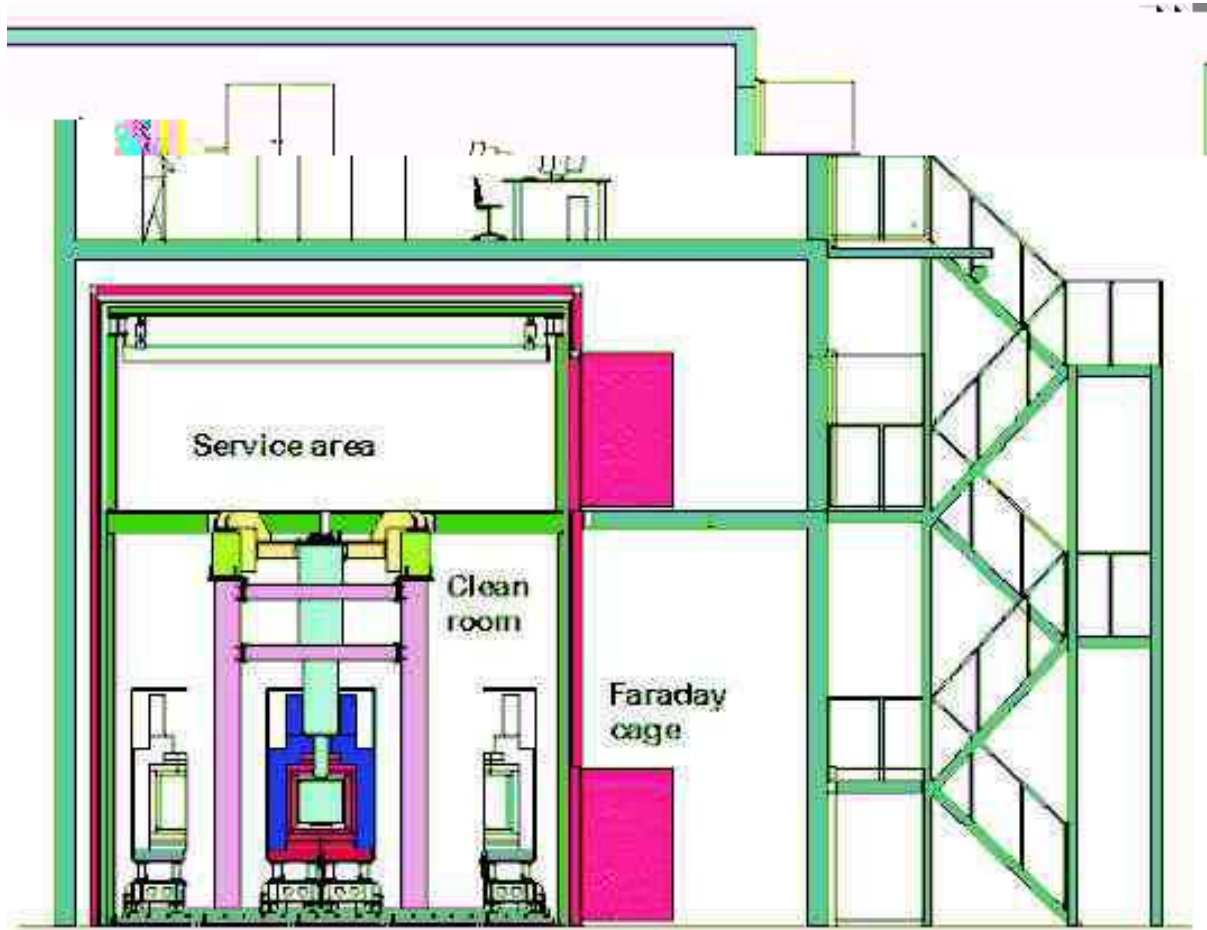


Figure 2: Cross section of CRESST building in Hall B. The external shielding is shown in both its open and closed positions.

on the low-background components of the experiment can be performed inside the cage. The cage is divided into two levels. The lower level is equipped as a clean room with a measured clean room class of 100 to protect the low-background components. The external lead and copper shields are in two closely fitting halves, each supported on a “wagon” on rails, so that the shielding can be opened without handling the individual pieces. The entire shielding is enclosed in a gas-tight Radon box that is flushed with N_2 and maintained at a small overpressure. In its retracted position (shown in Fig. 2) the shielding is outside the dilution refrigerator support structure but still inside the clean room and sufficient room is then available to disassemble the cold box.

Entrance to the clean room is through a changing room external to the Faraday cage (not shown in Fig. 2). The upper level of the Faraday cage is outside the clean room and allows access to the top of the cryostat for servicing and to the electronics. To save on floor space in Gran Sasso, the counting room and a laminar-flow work space for handling the detectors is placed on top of the Faraday cage. All of this equipment is inside a building in Hall B.

The original installation used a prototype cold box, not made of radiopure materials. The purpose of the prototype was to test the cryogenic functioning of the design and to provide a well-shielded environment for completing the development of the 262 g detectors. At the end of 1998 the prototype cold box was replaced by a radiopure version of the same design. After machining, the new cold box was cleaned by electropolishing and subsequent rinsing with high-purity water. The pieces were then brought to Gran Sasso in gas-tight transport containers made of PE and flushed with nitrogen.

2 Detectors and results of Phase I

2.1 Sapphire cryogenic calorimeters

The detectors we have developed [1, 2, 3, 4] consist of a dielectric crystal in which the particle interaction takes place, and a small superconducting film evaporated onto the surface, serving as a thermometer. The detector is operated within the superconducting-to-normal transition of the thermometer, where a small temperature rise ΔT of the thermometer leads to a relatively large rise ΔR of its resistance. The ΔT induced by a particle in the energy range of interest for dark matter is much smaller than the width of the transition, so that there is an approximately linear relation between ΔT and ΔR .

We have found [5] that the energy deposited by the particle does not thermalize in the sapphire crystal. Instead, to good approximation, the high frequency phonons created by an event spread throughout the crystal and reflect at the surfaces until they are directly absorbed in the superconducting film. Thus the energy resolution is only moderately dependent on the size of the crystal, and scaling up to large detectors is feasible.

The technique can be applied to a variety of materials. The detectors employed in Phase I of the CRESST experiment in Gran Sasso used 262 g sapphire (Al_2O_3) absorbers and tungsten (W) thermometers operating near 15 mK. The 262 g sapphire detectors were developed

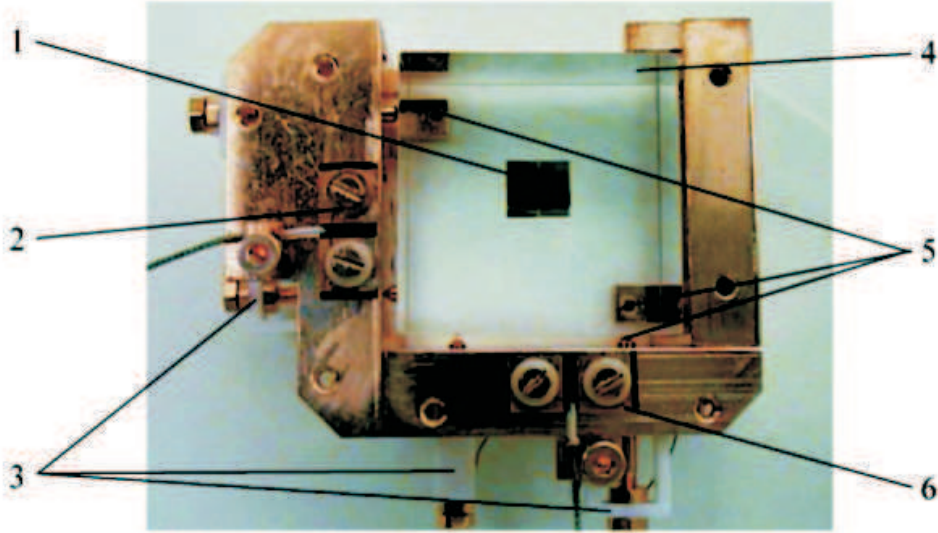


Figure 3: Photograph of a 262 g sapphire detector. The transparent sapphire crystal (4) is in the center. The other visible components are: (1) tungsten thermometer, (2) holder pads with screw contacts for connecting to the heater circuit, (3) plastic springs, (5) sapphire balls, (6) holder pads with screw contacts for connecting to the SQUID read-out circuit.

by scaling up a 32 g sapphire detector [4]. Due to optimized design, and because of the non-thermalization of the phonons, this scaling-up was achieved without significant loss in sensitivity.

Fig. 3 shows a 262 g sapphire detector mounted in its copper holder. The $4 \times 4 \times 4.1 \text{ cm}^3$ crystal rested thermally insulated on supports attached to the holder. In the original design, these supports were sapphire balls. Some of the supports were fixed and others were on pins loaded with plastic springs.

The detector used for dark matter limits had a W thermometer of size $3 \text{ mm} \times 5 \text{ mm}$. The electrical and thermal connections to the detector are shown in Fig. 4. Thermal contact between the holder and the detector was provided by gold wires of diameter $25 \mu\text{m}$ bonded to the Cu holder and to a gold contact pad in the middle of the W thermometer. The copper holder was thermally connected via the cold finger to the mixing chamber of the dilution refrigerator, which was stabilized to a temperature of 6 mK. The electrical connection to the detector was made by superconducting Al wires bonded to Al pads on each end of the thermometer and to isolated contact pads on the holder. To avoid radioactive solder joints, the superconducting wires from there to the external readout circuit were screwed to the contact pads. The resistance of the thermometer ($\sim 0.1 \Omega$) was measured by passing a constant current I_0 through the readout circuit in which the thermometer was in parallel with a small ($\sim 0.05 \Omega$) resistor and the input coil of a dc-SQUID (Fig. 5). A rise in the thermometer resistance was then measured via the current rise through the SQUID input coil.

In a separate circuit, a heater to control the temperature of the detector was provided by

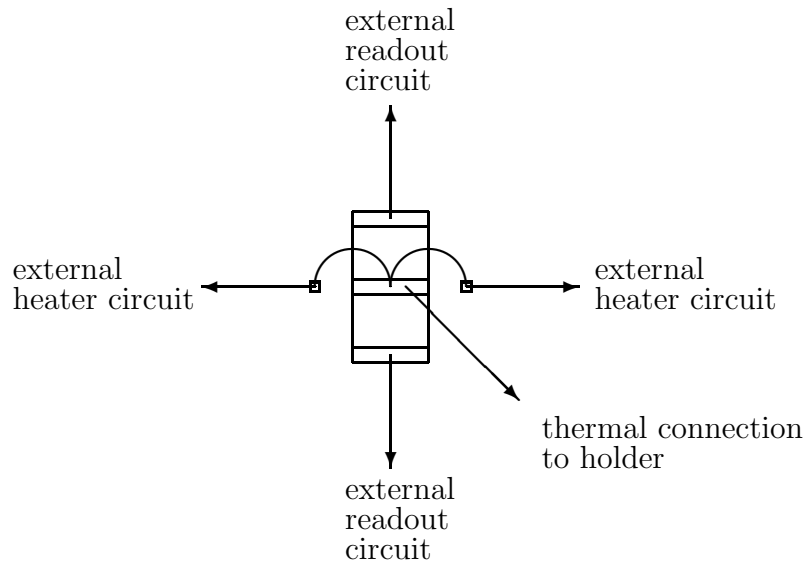


Figure 4: Thermal and electrical connections to thermometer.

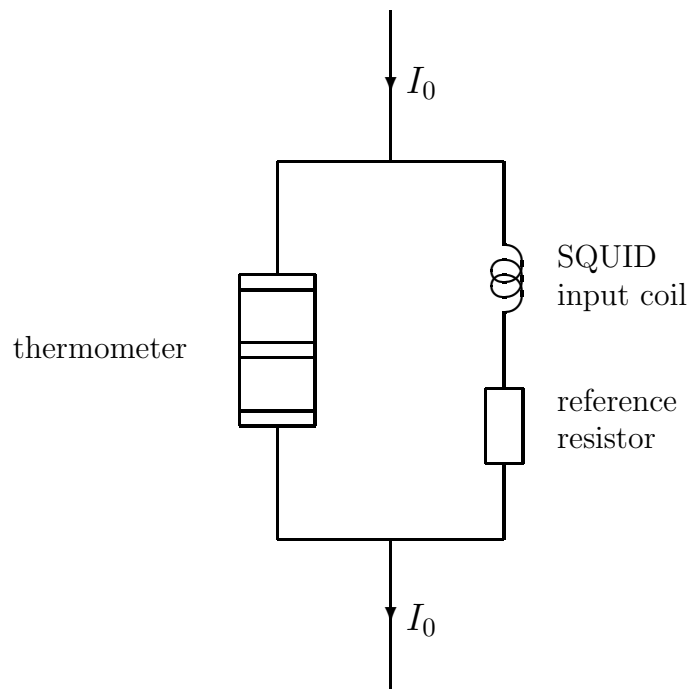


Figure 5: Readout circuit to measure the resistance of the thermometer.

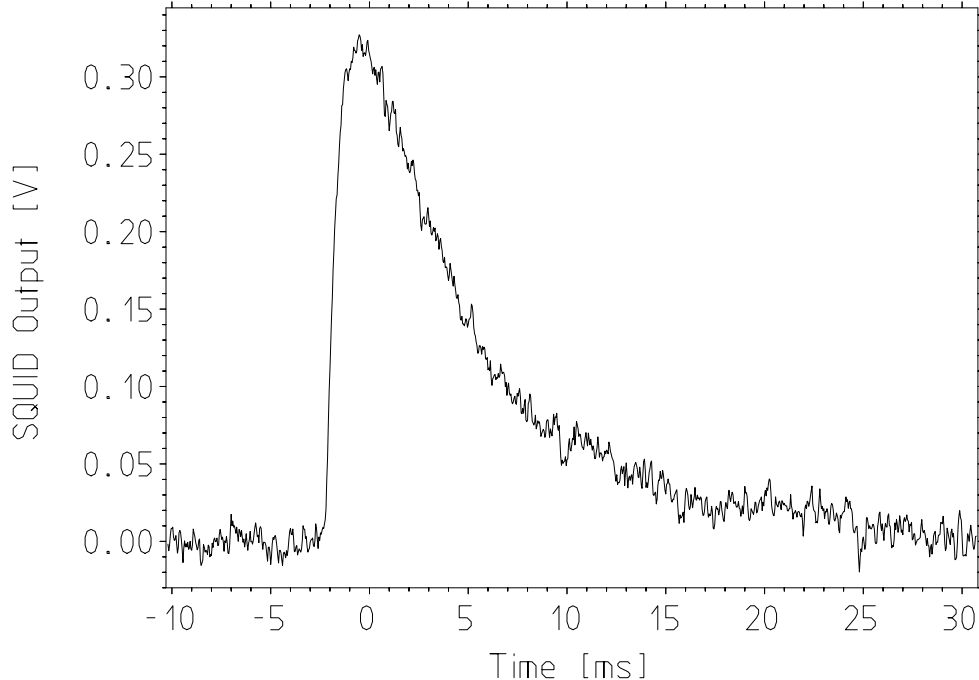


Figure 6: Typical measured pulse of about 6 keV.

a ~ 5 mm long $25\ \mu\text{m}$ diameter gold wire which was bonded to the gold pad in the center of the W thermometer and two very small Al contact pads on the sapphire crystal to either side of the thermometer. External connections to the two small Al pads were used to apply a controlled voltage across this gold wire. To avoid interaction between the heater circuit and the readout circuit, the place where they connect – the bond spot of the gold wire – was made as small as possible and its long axis was perpendicular to the direction of current flow in the thermometer. The thermometer temperature was kept constant between pulses using the baseline of the SQUID output voltage as the temperature indicator and regulating the voltage to the heater under computer control using a proportional integral algorithm. The heater was additionally used to inject short heat pulses for monitoring the long term stability of the energy calibration and for measuring the trigger efficiency close to threshold.

For the data-acquisition system, the output voltage of the SQUID electronics was split into two branches. One was shaped and ac-coupled to a trigger unit and the other passed through an anti-aliasing filter and was dc-coupled to a 16-bit transient recorder. The time base of the transient recorder was chosen to be $40\ \mu\text{s}$, which provided about 20 samples in the rise time of the pulse. The record length of 1024 time bins included a “pre-trigger” region of 256 bins, to record the baseline before the event, and a “post-trigger” region which contained the pulse (Fig. 6). The transient recorder data for each triggered event were written to disk for off-line analysis. After each trigger there was a dead time of ~ 25 ms to allow time for the readout and the next pre-trigger region. Pulses arriving in another detector within half of the post-trigger period of the detector which triggered first were also recorded, including the time delay with respect to the first trigger.

2.2 Data taken in Gran Sasso

The sensitivity and size of the 262 g detectors meant that they could only be meaningfully tested in a low-background environment. This was first done in our setup in Gran Sasso using the prototype cold box of normal copper. Using active thermal feedback, an energy resolution of 133 eV (FWHM) at 1.5 keV for X-rays was achieved [6]. This active feedback was not used in our dark matter run, and without it the resolution at 1.5 keV is more typically 230-330 eV [7].

During 1999, a first series of measurements with four 262 g detectors under low-background conditions was performed in the new radiopure cold box. The measured background was much higher than expected. It was time-dependent and not Poissonian, indicating that it was not caused by radioactivity. The origin of this background was investigated in a series of runs and finally identified as the spontaneous formation of microscopic cracks in the sapphire crystal at the points where it was supported by sapphire balls. Due to the extremely small contact area of the balls, an excessive pressure resulted from the force needed to tightly hold the crystal. In the spring of 2000 the balls were replaced by plastic stubs with a larger contact area (3 mm diameter) and the spurious background completely disappeared. The use of these stubs did not lead to a noticeable loss of sensitivity, despite their larger contact area.

To study the background and obtain dark matter limits, several runs were performed in 2000, with the longest one lasting about 3 months. The high reliability, long-term stability and up-time during these runs demonstrated convincingly the suitability of such a system for dark matter searches.

In October 2000 the shaping of the trigger signal was optimized and a lower trigger threshold was obtained. A week of data were taken under these conditions. Due to this lower threshold, the dark matter limits obtained from these data are better than those from the previous longer runs, and it is these data which we discuss further. The data consist of a 10-hour calibration run with an external ^{57}Co source, 138.8 hours of data without source and finally another calibration run. The 138 hour run will be used to set our dark matter limits.

2.3 Detector monitoring and calibration

The performance of the detector was monitored by heater pulses injected into the small heater wire bonded to the W thermometer. These are produced by a voltage pulse from a pulser module, with the shape adjusted to create a detector response similar to that caused by a particle interaction. A pulse was sent every 30s throughout both dark matter and calibration runs. The height of the pulses was varied to cover the whole dynamic range, with more pulses in the low energy region. This method provides a monitor of the stability of the detectors, an extrapolation of the energy calibration over the whole dynamic range, and a measure of their trigger efficiency as a function of deposited energy.

The individual detectors varied in their response, with detector #8 (numbered by order of fabrication) having a lower threshold and thus giving the best dark matter limits. The

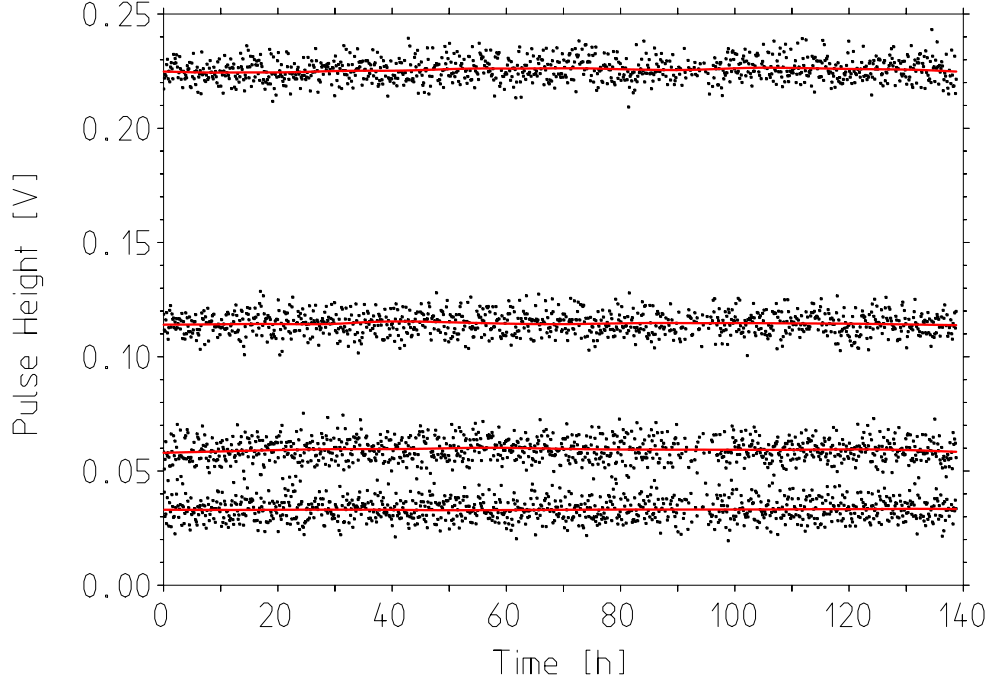


Figure 7: The measured pulse height of detector #8 as a function of time during the dark matter run for the heater pulses of energy 0.58, 1.04, 2.04, and 4.08 keV. The detector is seen to be stable to within the resolution. The fitted lines are used to calculate the response function at the time of event pulses as shown in Fig. 8.

trigger efficiency of this detector was measured to be 100% down to an energy of 580 eV throughout the data used to extract the dark matter limits. The stability of detector #8 during the dark matter run can be seen in Fig. 7, where the response to heater pulses is shown.

To calibrate the energy scale a ^{57}Co source (122 and 136 keV γ lines) was inserted inside the shielding via a removable plug, illuminating the cold box from below. Data were taken with this source along with the heater pulses. Comparison of the pulse heights from the source and heater pulses provides an absolute calibration of the heater pulses in terms of equivalent γ energy. The amplitude of each pulse was determined by fitting it to a template. This avoids the bias of picking the highest point of suitably filtered pulses, which is systematically pulled by noise fluctuations to larger values. The absence of any bias is important for a precise definition of the threshold. It was therefore checked by fitting empty base lines randomly sampled during the whole data taking period. The resulting distribution peaked without any bias at (-0.0019 ± 0.003) keV.

The templates were made by averaging many pulses from the same heater pulse voltage. A separate template was made for each heater energy, and for source pulses around the Compton edge (30-35 keV). To extrapolate the energy calibration over the whole dynamic range, we used the heater pulses and plotted their fitted amplitude versus the injected energy (Fig. 8). These data were fit with a polynomial function to give the detector response as a function of deposited energy.

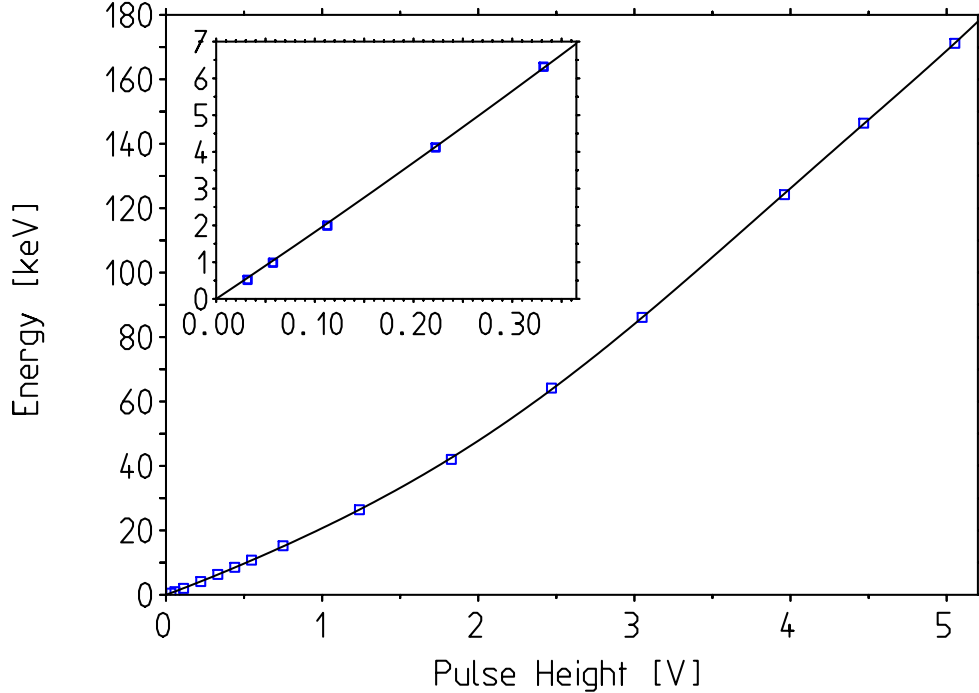


Figure 8: The pulse heights for detector # 8 for each injected heater pulse energy calculated from the lines in Fig. 7 are shown as points. The curve is the fitted polynomial which is used as the response function. The insert is an enlargement of the low energy region.

For the dark matter data, the response function determined above was used to convert each recorded event pulse to energy in each time bin. An optimal filter was then used on this converted pulse to determine the pulse height. This gave a slightly better resolution than a template fit. A comparison to the template fit showed that the optimal filter applied to the linearized pulses does not introduce an energy bias. The resulting spectrum for the dark matter run is shown as the upper histogram in Fig. 9.

The reliability of the energy calibration method to low energy was checked with a dedicated run where a low activity ^{57}Co source was mounted inside the cryostat directly facing the crystals. Besides the 122 and 136 keV γ emission lines, this source gave a 14.4 keV γ line and a 6.4 keV Fe X ray line. The source was chosen to be very weak to reduce the chance of contamination so that one week run gave only a small number of counts in the 14.4 and 6.4 keV lines. After applying the standard calibration method of extrapolation from the 122 keV line as described above, the measured energies for the 14.4 and 6.4 keV lines were $15.16^{+0.09}_{-0.09}$ keV and $6.70^{+0.07}_{-0.05}$ keV, respectively, with the fit errors corresponding to 90 % CL. Our calibration procedure puts the 14.4 and the 6.4 keV lines 5.3 % and 5.4% too high. Since it is the lower energies which most affect our dark matter limits, this tendency to shift events up in energy will put our limits on the conservative side.

2.4 Energy spectrum from dark matter run

The data used to set dark matter limits were taken during a week in October 2000, with a few short interruptions to re-fill the cryostat with liquid helium. The total run time was 138.8 hours, of which 0.6 hours is dead time following triggers.

To avoid reliance on the detailed behaviour of the trigger efficiency at very low energies a software threshold of 600 eV was used. There were 374 events from the software threshold to 20 keV.

Events in coincidence in two or more detectors cannot be due to WIMP interactions, and so can be discarded. The time difference distribution between events showed a clear coincidence peak with a width of about 0.4 ms and long tails extending to about 2 ms for very low detected energies. The coincidence cut was set at ± 4 ms, removing 73 events. Considering that only two detectors were active in this run and only one out of six faces was facing the other crystal, the coincidence rate of almost 20% is surprisingly high.

The pulse shape of the remaining 301 events was then examined. Some of the events were spurious, induced by mechanical vibration or electronic noise, showing an abnormal pulse shape. Particle interactions can also produce distorted shapes when the energy deposit is high and beyond the detector's dynamic range. To judge the correctness of the pulse shape, each event was fitted to a template and the r.m.s. deviation calculated. A cut on this deviation was chosen to be conservative and have a retention efficiency of essentially 100% at all energies for good events. Its efficiency was tested with heater pulses, resulting in only 1 out of 1032 of the 580 eV heater pulses being discarded. A second test with the calibration source gave that only 0.22% of the events were discarded. After the pulse shape cut 265 events remain. These are shown as the lower histogram in Fig. 9.

The final spectrum for detector #8 is shown again in Fig. 10. In the energy range from 15 to 25 keV the background is (0.73 ± 0.22) counts/kg/keV/day and drops to about 0.3 counts/kg/keV/day at 100 keV.

The spectrum shows a peak at about 5.9 keV with (7.0 ± 1.2) counts/day. The position of the peak suggests a contamination with ^{55}Fe in the vicinity of the crystal. ^{55}Fe emits Mn X-rays at 5.9 keV with no γ 's and was indeed used as a source for characterizing the performance of the detectors. The spectra measured with other detectors are very similar with nearly the same count rates in both the peak and the continuous part of the spectrum.

2.5 Limits on WIMP dark matter

The analysis for dark matter limits of the two possible WIMP interaction cross sections for our sapphire detectors, i.e. spin-independent $\sigma_{\text{scalar}}^{W-N}$ and spin-dependent $\sigma_{\text{axial}}^{W-N}$ WIMP-nucleon cross sections, searches for the cross section which is just large enough that the amount of WIMP events becomes inconsistent with the measured spectrum at a given confidence level (here 90% CL). No general algorithm for such an analysis has been found in the literature. Therefore we developed two conceptually independent approaches to be described below and checked for consistency of the results.

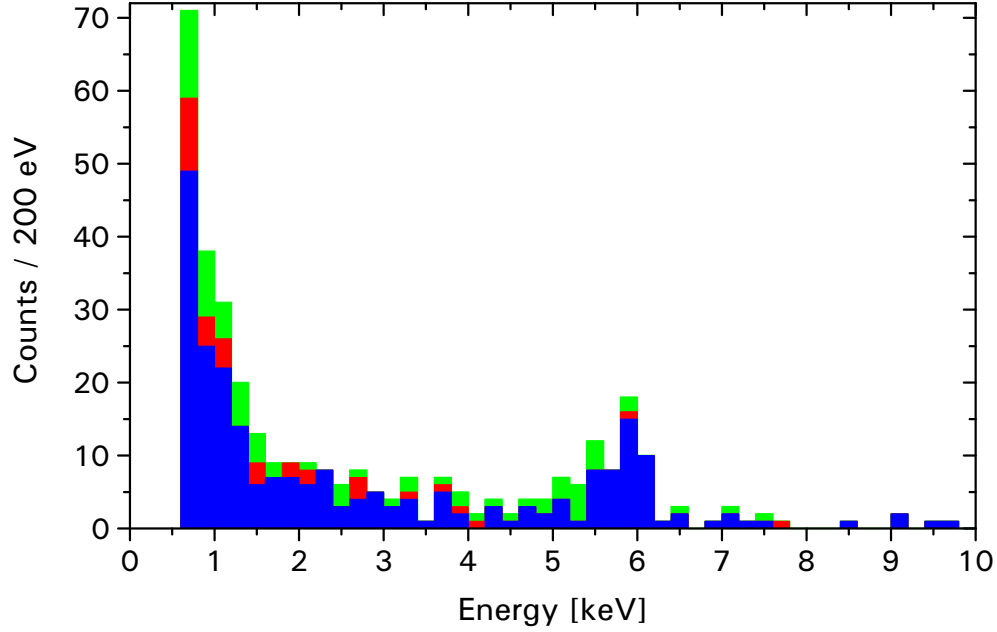


Figure 9: Energy spectrum of events in the dark matter run (without source) in 200 eV bins. The upper histogram shows the uncut data, the middle histogram the data after coincident events are rejected, and the lower histogram after the pulse shape cut.

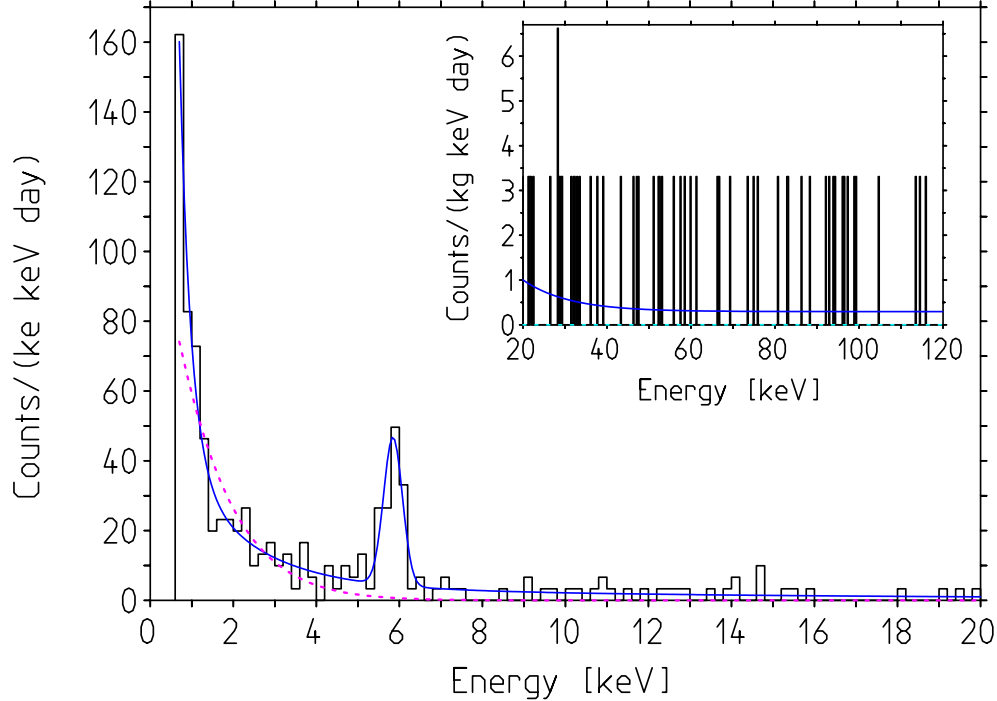


Figure 10: Energy spectrum of detector #8 during the dark matter run (1.51 kg days) in 200 eV bins. The insert shows the spectrum at higher energies. The fully drawn curve is an empirical fit to the experimental spectrum which serves for extracting dark matter limits. For illustration a 5 GeV WIMP excluded at 90% C.L is shown as a dashed curve.

For calculating the energy spectrum of nuclear recoils from elastic collisions between WIMPs and the nuclei of the detector we use formulas from the extensive reviews [8, 9] for a truncated Maxwell velocity distribution in an isothermal WIMP–halo model. The parameters which have been used are summarized in table 1. For the spin dependent interaction channel only the ^{27}Al nuclei with a spin of 5/2 and 100% natural isotopic abundance contribute, while for spin independent interaction Al and O nuclei both contribute with a rate proportional to A^2 .

Table 1: List of parameters used for calculating WIMP spectra

Parameter name	value
WIMP velocity distribution	270 km/s
Escape velocity	650 km/s
Earth relative velocity	230 km/s
WIMP local halo density	0.3 GeV/cm ³

The total WIMP–nucleus scattering cross section $\sigma(q)$ at finite momentum transfers q is parameterized as $\sigma(q) = \sigma_0 F^2(q)$, where σ_0 is the cross section at zero momentum transfer and $F(q)$ is the form factor which accounts for the loss of coherence at larger momentum transfers. The Helm form factor [10] with the modifications proposed in [8] has been selected for both interaction channels. For small nuclei like ^{27}Al the momentum transfer is small for all WIMP masses, and details of the form factor have negligible effect on the resulting exclusion plot. Therefore the selected form factor is adequate for both interaction channels. The energy resolution at the 5.9 keV peak in Fig. 10. is $\delta E = (572 \pm 90)$ eV (FWHM), whereas the resolution of the Fe K_α peak at 6.4 keV from the internal calibration source is (200 ± 50) eV in agreement with the energy resolution of the heater pulses. At the 122 keV peak of the calibration source the resolution degrades to about 5 keV. To account for the finite energy resolution of the detector the recoil spectrum was convolved with a Gaussian with an energy dependent full width at half maximum of $\delta E = \sqrt{a^2 + b^2 E^2}$. With $a=0.52$ keV and $b=4.1$, this gives $\delta E = 0.57$ keV and $\delta E = 5$ keV at $E=5.9$ keV and $E=122$ keV, respectively. We further assumed a quenching factor of 1, i.e. 100% of the nuclear recoil energy is detected in the phonon readout channel. An experimental proof of this plausible assumption does not exist up to now for our sapphire detectors. However, quenching factors close to 1 have been measured with other cryogenic detectors [12].

The analysis procedure which has been used to obtain the exclusion curves is Fig. 12 and Fig. 13 works as follows: After calculating the shape of the energy spectrum for a given WIMP mass, σ_0 which is the scale factor for the intensity of the WIMP expectation, is determined by a maximum–likelihood comparison of the calculated WIMP spectrum with the measured energy spectrum. The analysis is aiming to find the amount of WIMP events that just too large to be hidden under the measured spectrum. Some energy intervals (typically close to the threshold) are more effective than others for constraining the existence of a WIMP signal in the data. Therefore, it is reasonable to select these energy intervals and use them to give the most stringent exclusion limits on a WIMP signal that can be obtained from the data.

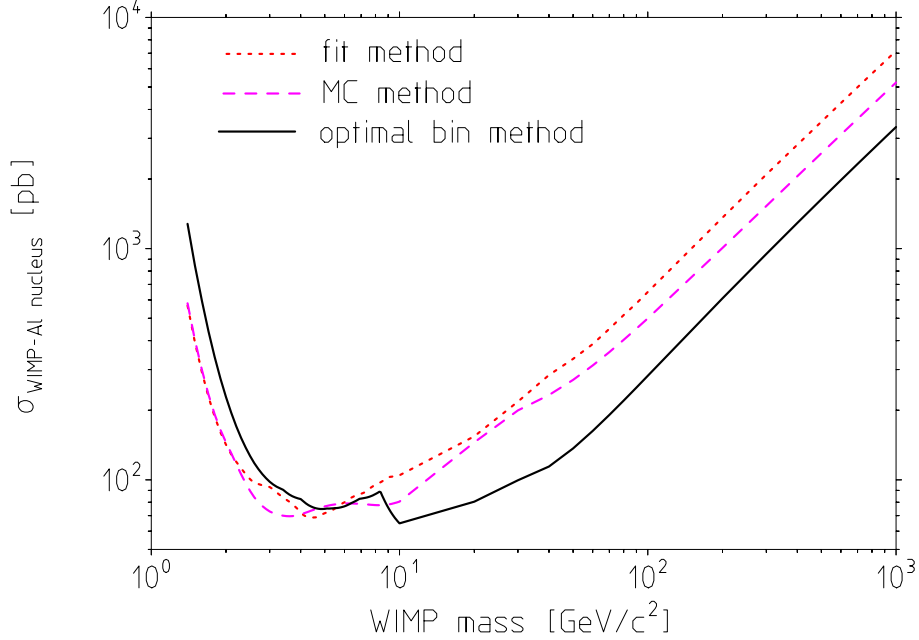


Figure 11: Comparison of different statistical methods to extract exclusion limits. Shown is the WIMP- ^{27}Al nucleus cross section limit (90 % CL) obtained with 3 different methods. The MC-method was selected to extract the limits shown in Fig. 13 and Fig. 12.

We performed such a search, using a sliding, variable-width energy window with a smallest width of 1.2 keV. A similar method was used in [13, 14, 16]. Since the method tends to pick a 'lucky' downward fluctuation in the data, especially in a low count rate spectrum, it may have a significant statistical bias. Therefore we have investigated the selection bias with two simple alternative methods.

In the first method we fit the spectrum with an empirical function B as shown in Fig. 10 which results in a likelihood of $\mathcal{L} = \mathcal{L}_0$. Without a WIMP contribution this function just describes the background. When a small WIMP signal S is first added, which is everywhere smaller than the fit function, then with a re-definition of the background to $B' = B - S$ we can achieve to leave \mathcal{L} unchanged. With increasing σ_0 , when S starts to exceed the fit function in the first energy bin, this compensation would require a negative background and in this bin the function to compare with the data is then the WIMP signal and \mathcal{L} starts to decrease. The cross section excluded at 90% CL is obtained when $\mathcal{L} = \mathcal{L}_0 - 1.28^2/2$ is reached.

The second method starts from the same empirical fit of the data and then uses this fit function as the poissonian mean in a Monte Carlo calculation of a large number of synthetic spectra. These spectra are different statistical realizations of the measurement when the fit function is adequate for describing the data. The same function is then fit to each synthetic data set to probe the statistical variation of the fit curve. Then, from each fitted curve σ_0 is determined such as to make the WIMP signal just large enough to explain the fit curve in one energy bin. The σ_0 which is excluded at 90% CL is then obtained as the cross section for which 90 % of the values determined from all fits are below. Finally, the adequacy of the fit function can be inferred from a comparison of the likelihood from the fit of the data with

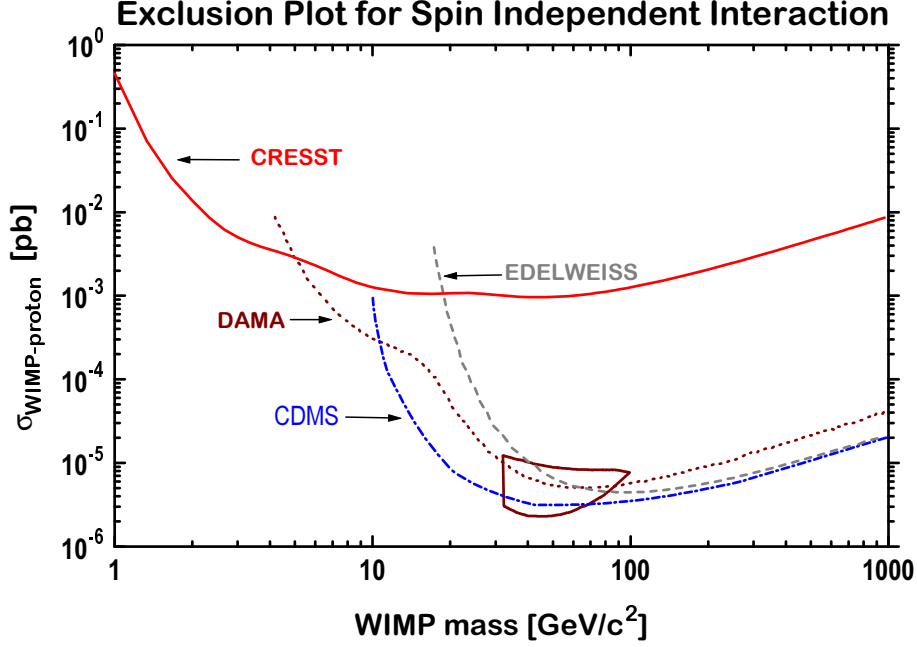


Figure 12: Equivalent WIMP-nucleon cross section limits (90% CL) for spin-independent interaction as a function of the WIMP mass for 1.51 kg days exposure of a 262g sapphire detector. For comparison DAMA NaI limits with pulse shape discrimination [17], CDMS limits with statistical subtraction of the neutron background [19], limits from the UK dark matter search [18] and from the EDELWEISS WIMP search with a heat and ionization Ge Detector [20] are also shown together with the allowed region at 3σ CL for a WIMP r.m.s velocity of 270 km/s from the DAMA annual modulation data [25].

the likelihoods from the fits of the synthetic data sets. For the curve shown in Fig. 10, 49.1% of the synthetic likelihood values are larger, indicating a perfect choice of the fit function.

The results of these methods are compared in Fig. 11. At low WIMP masses the optimal bin method yields weaker limits. This is connected with the restriction to a 1.2 keV minimal width of the sliding bin which is quite large for very low WIMP masses for which the optimal bin starts at threshold. For WIMP masses above 10 GeV on the other hand the optimal bin is searched in relatively wide region with low statistics which results in a large selection bias. For a WIMP mass from 30 GeV to 1000 GeV for example the region from 22.7 keV to 26.3 keV with no counts inside is selected as the optimal bin. To avoid this bias we have chosen the MC method. The small difference between MC and fitting method still needs further investigation and therefore we consider the results presented here still as preliminary.

In order to compare our results to those of other experiments, we have to normalize the obtained WIMP-nucleus cross sections (for spin-dependent, axial, and spin-independent, scalar, interactions) to WIMP-nucleon cross sections. Following [8, 9], the normalization for the scalar interaction channel is straight forward and yields the results shown in Fig. 12. The scalar channel is not very favourable for a target with light nuclei like sapphire, containing aluminium and oxygen, due to the crucial A^2 coherence factor, especially for higher WIMP masses. That will change with the CRESST-II detectors as explained in the next section.

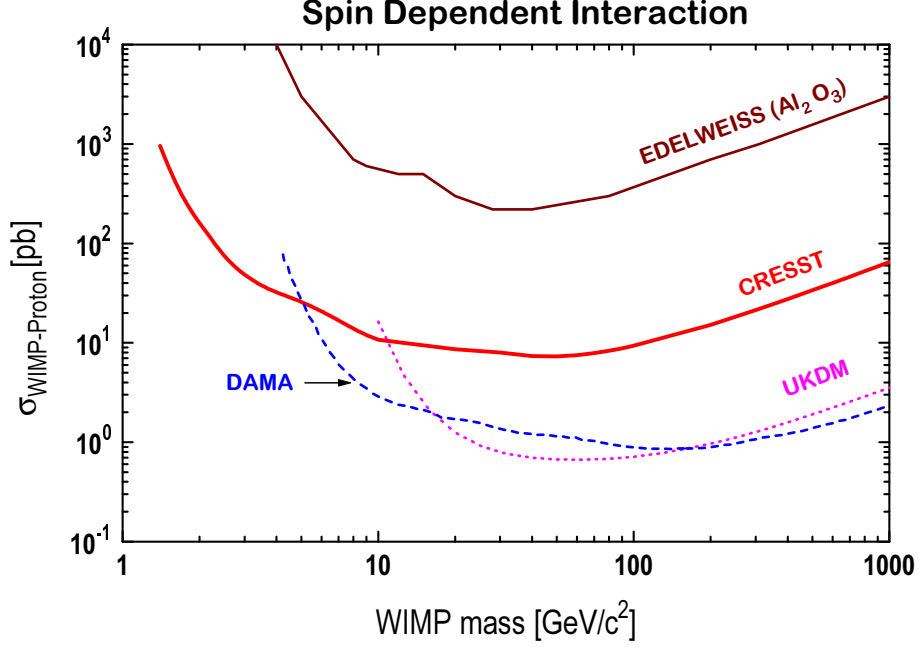


Figure 13: Equivalent WIMP-proton cross section limits (90% CL) for spin-dependent interaction as a function of the WIMP mass from 1.51 kg days exposure of a 262 g sapphire detector. For comparison we show limits from the EDELWEISS dark matter search with cryogenic sapphire detectors [16], from DAMA with NaI detectors using pulse-shape discrimination [17], and from the UK dark matter search with NaI detectors [18].

For axial interactions, only ^{27}Al has to be considered, since it has spin 5/2. The spin dependent total cross section at zero momentum transfer in the notation of Ref. [15] is given by

$$\sigma_0 = 4G_F^2 \mu_A^2 C_A, \quad (1)$$

where the WIMP-target reduced mass μ_A is given by $\mu_A = m_A m_\chi / (m_A + m_\chi)$ for WIMP mass m_χ and target nucleus mass m_A . The spin factor C_A is given by

$$C_A = \frac{8}{\pi} [a_p \langle S_p \rangle + a_n \langle S_n \rangle]^2 \frac{J+1}{J}. \quad (2)$$

where a_p and a_n are (WIMP-type dependent) effective WIMP-proton and WIMP-neutron couplings and $\langle S_{p,n} \rangle$ are the expectation values of the proton and neutron spins within the nucleus with total nuclear spin J . The limit σ_0 obtained for the WIMP- ^{27}Al nucleus cross section can be translated into a limit for the WIMP-proton cross section by the conversion

$$\sigma_{WIMP-p} = \sigma_0 \times \frac{\mu_p^2}{\mu_A^2} \times \left(\frac{C_p}{C_A} \right). \quad (3)$$

However, this normalization turned out to be nontrivial as the recent discussions in the literature has shown [8, 15]. The 'conventional' procedure relied on the odd-group model which uniquely determines the spin factor for a given material, see e.g. Tab. 3 in [8]. Furthermore, the normalization conveniently cancelled the WIMP model dependencies coming from particle physics. That can be directly seen from the spin factor in Eq.2, where the $a_{p,n}$ parameters contain the particle physics model-dependencies.

For free nucleons the spin factor is [15]

$$C_{p,n} = \frac{8}{\pi} \times \frac{3}{4} \times a_{p,n}^2. \quad (4)$$

The odd-group model implies that for nuclei with unpaired protons or neutrons either $\langle S_p \rangle$ or $\langle S_n \rangle$ is zero in Eq. 2, respectively. Therefore, when normalized to the unpaired nucleon the model dependent $a_{p,n}$ factors conveniently cancelled in Eq.3. According to shell model calculation (see [9, 8, 15] and references therein; for ^{27}Al , see [11]) strict p- or n-type nuclei do not exist and in general both, $\langle S_p \rangle$ and $\langle S_n \rangle$ contribute and can even interfere in Eq. 2.

As proposed in [15], an experiment should therefore publish results separately for the p-type part and the n-type part for their particular nucleus. However, in order to be able to compare our results to already published limits, we applied the odd-group model spin factor, although the value in [8] for aluminium is outdated. The more recent spin factor using the numbers from [11] would result in a factor 1.9 reduction of the whole exclusion curve to lower cross sections, in case one neglects the neutron part for the spin factor as described in [15]. One should be aware, however, that using the odd group model approach any comparison to n-type nuclei like ^{73}Ge becomes very problematic. Such a comparison inevitably involves model-dependencies (see e.g. the discussion in [8] and their Tab. 4). All limits in Fig. 13 consequently come from p-type nuclei (aluminium, sodium and iodine). As can be seen in Fig. 13, we improve existing limits in the low-mass region.

3 Plans for Phase II

3.1 Scintillating calorimeters

Passive techniques of background reduction – the deep underground site, efficient shielding against radioactivity of the surrounding rocks, and use of radiopure materials – cannot completely eliminate background from radioactive contaminants inside the detectors and their surroundings. β and γ absorption produce electron recoils, whereas WIMP and neutron scattering produce nuclear recoils. Therefore a significant improvement in sensitivity can be achieved if, in addition to the usual passive shielding, the detector can distinguish electron recoils from nuclear recoils and reject them.

It is well known that at room temperatures nuclear recoils in scintillators produce much less scintillation light than electron recoils. Thus the combination of a scintillator, measuring light, and a cryogenic detector, essentially measuring total energy, can discriminate between nuclear and electron recoils by using the ratio of detected light to thermal energy. We have investigated the light output of several scintillators at mK temperatures, concentrating on inorganic intrinsic scintillators since their scintillation efficiency usually increases at lower temperatures. All scintillators so far tested (BGO, BaF₂, PbWO₄, CaWO₄) appear to function adequately at mK temperatures.

For an initial test [21] of a scintillating calorimeter we chose CaWO₄. The test setup consisted of two independent detectors. Each one was of the CRESST type: a tungsten superconducting phase transition thermometer with SQUID readout. The scintillating absorber

and phonon detector was a 6 g CaWO_4 crystal. The light detector was a sapphire wafer, coated with silicon on one side to enhance light absorption. The CaWO_4 crystal was irradiated with the 122 keV and 136 keV photons from a ^{57}Co -Source and simultaneously with the β spectrum from a ^{90}Sr source, with the two sources contributing about equally to the count rate. In addition an americium-beryllium source provided neutrons. The trigger was given by the phonon detector.

Fig. 14 shows a scatter plot of the pulse heights observed in the light detector versus the pulse height observed in the phonon detector. The pulse height has been converted to energy using the 122 keV photon peak in both detectors. The plot shows two well-separated bands. The lower band is caused by neutron-induced nuclear recoils while the diagonal band is caused by electron recoils induced by γ 's and β 's. Electron and nuclear recoils can be clearly distinguished down to a threshold of about 10 keV. From the ratio of pulse height light / pulse height phonons for the two bands, a quenching factor (the ratio of the light output for electrons to that for nuclear recoil) of 7.4 can be inferred. The leakage of electron recoils into the nuclear recoil band determines the effectiveness of the electron recoil rejection. If we use a quality factor as defined in Ref. [22], a detailed evaluation together with data taken without neutrons, we find a rejection factor of 98 % in the energy range between 10 keV and 20 keV; 99.7 % in the range between 15 keV and 25 keV; and better than 99.9 % above 20 keV.

The simultaneous light and phonon measurement has several advantages over the simultaneous measurement of charge and phonons, which is another method of the same type. In the measurement of charge and phonons electrical contacts always produce a dead layer on the surface, which causes surface events, especially electrons from outside, to leak into the nuclear recoil band. As our measurements with electrons clearly show, this problem does not exist with light detection. Also light collection does not suffer from problems such as space charge build up, field inhomogeneities or phonons produced by drifting the charges. Thus many effects are absent which in charge/phonon measurement can cause leakage of electron recoils into the nuclear recoil band. As a result the background suppression efficiency of the light/phonon detection is excellent. It works equally well for photons and electrons, thus avoiding particle dependent systematic uncertainties in discrimination. Furthermore the large quenching factor of the CaWO_4 gives a very effective separation of nuclear recoils from electron recoils.

The possibility of using different scintillators with different target nuclei, which is possible with CRESST technology, gives a powerful handle for understanding and reducing backgrounds. Even the neutron background, always considered to be the ultimate limitation for such systems, could be understood by varying the target nuclei.

For a dark matter search, detector masses of several hundred grams per channel are needed. It is therefore necessary to scale up the 6 g detector used in the above tests without loss of performance. Since the device consists of two CRESST-type detectors, we are confident of being able to produce much larger detectors of similar performance by applying familiar techniques and optimizing the design.

For Phase II of CRESST we plan to install scintillating calorimeters with a total mass of about 10 kg, consisting of 33 modules of 300 g CaWO_4 crystals. This assembly will fit easily in the present cold box. However the number of SQUID readout channels has to be upgraded

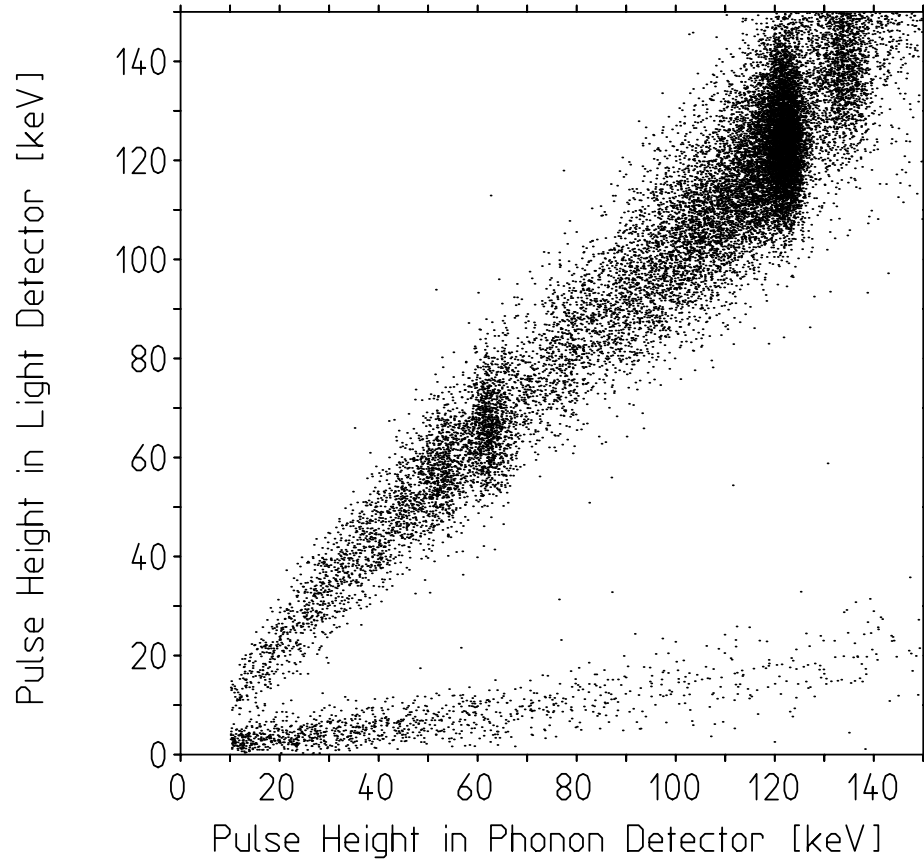


Figure 14: Pulse height in the light detector versus pulse height in the 6 g CaWO_4 phonon detector, measured while the detector was irradiated with photons, electrons, and neutrons. The lower band is caused by neutron-induced nuclear recoils, the diagonal band by recoils from photons and electrons.

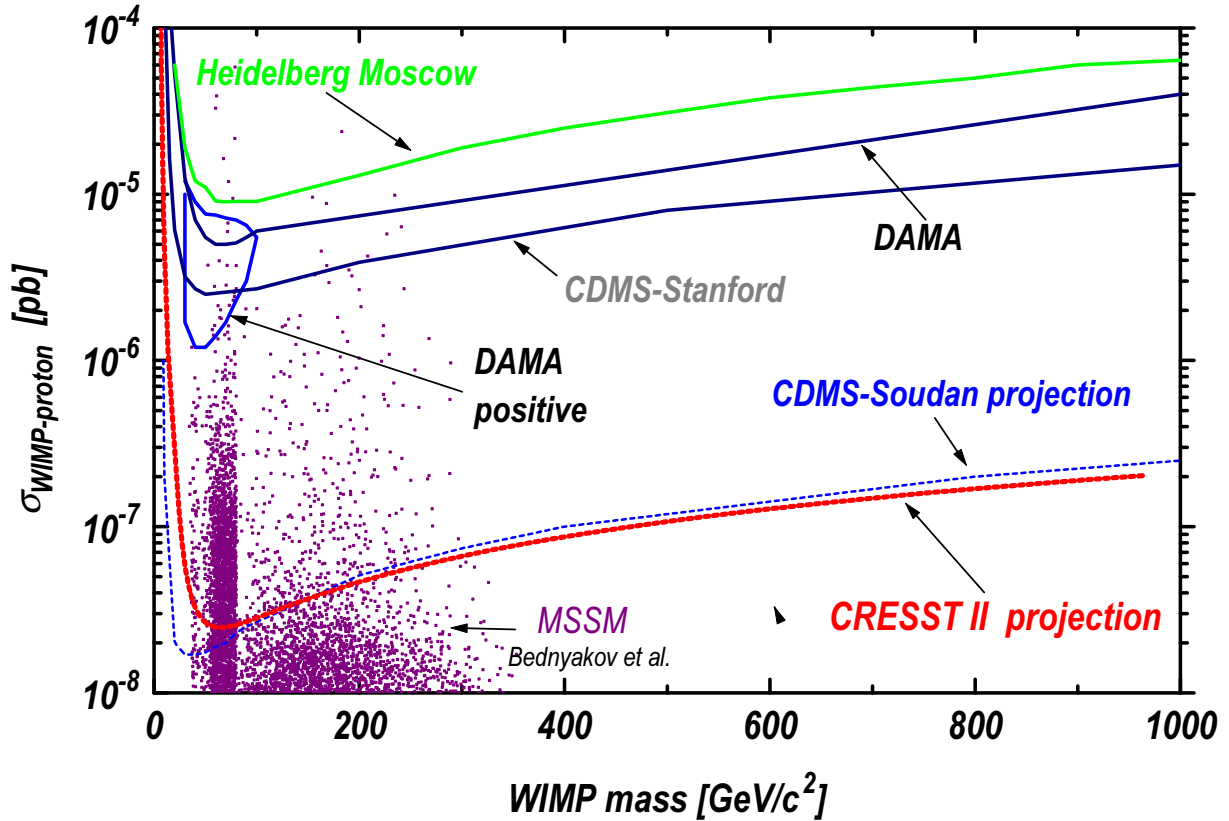


Figure 15: WIMP-nucleon cross section limits (90% CL) for spin-independent interactions as a function of the WIMP mass, expected for a 10 kg CaWO_4 detector with a background rejection of 99.7% above a threshold of 15 keV detector and 3 years of measurement time in the CRESST set-up in Gran Sasso. For comparison the measured limit from the Heidelberg-Moscow ^{76}Ge experiment [23], the DAMA NaI limits [24] and contour for positive evidence [25], the CDMS Stanford limit [19] and the expectation for CDMS Soudan [26] are also shown. The scatter plot shows the expectations for WIMP-neutralinos calculated in the MSSM framework with non-universal scalar mass unification [27].

to 66. Additionally we plan to install an external muon veto and a passive neutron shield. These upgrades are being implemented during 2001 as part of our move from Hall B to Hall A of Gran Sasso.

3.2 Expected dark matter sensitivity

The presence of the heavy tungsten nuclei make the new detectors particularly sensitive to a spin-independent interaction of WIMPs, for which the cross section profits from a large coherence factor of the order A^2 , where A is the number of nucleons. Combined with the strong background rejection, this gives good sensitivity down to low WIMP cross sections. Fig. 15 shows the expected sensitivity of Phase II, based on a background rate of 1 count/(kg keV day), an intrinsic background rejection of 99.7% above a recoil threshold of 15 keV, and an exposure of 30 kg years. For comparison the measured limits from the

Heidelberg-Moscow ^{76}Ge -diode experiment [23], the DAMA NaI experiment [24], the CDMS experiment at Stanford [19], and the projected sensitivity of CDMS at the Soudan mine [26] are also shown together with the contour for positive evidence [25] from the DAMA experiment.

In a 10 kg CaWO_4 detector, 60 GeV WIMPs with the cross section claimed in Ref. [25] would give about 46 counts between 15 and 25 keV within one month. A background of 1 count/(kg keV day) suppressed with 99.7% would leave 9 background counts in the same energy range. Thus a 10 kg CaWO_4 detector should allow a test of the reported positive signal with 1 month of measuring time.

This work was supported by the DFG SFB 375 “Particle Astrophysics”, the EU Network “Cryogenic Detectors” (contract ERBFMRXCT980167), BMBF, PPARC, and two EU Marie Curie Fellowships.

References

- [1] W. Seidel, G. Forster et al., Phys. Lett. B 236 (1990) 483.
- [2] M. Frank, D. Dummer et al., Nucl. Instr. Meth. A 345 (1994) 367.
- [3] P. Ferger et al., Phys. Lett. B 323 (1994) 95.
- [4] P. Colling, A. Nucciotti, C. Bucci et al., Nucl. Instr. Meth. 354 (1995) 408.
- [5] F. Pröbst, M. Frank et al., J. Low Temp. Phys. 100 (1995) 69.
- [6] O. Meier et al., Proc. LTD-8, Nucl. Instr. Meth. A 444 (2000) 350.
- [7] M. Sisti, O. Meier et al., Nucl. Instr. Meth. A 466 (2001).
(<http://wwwvms.mppmu.mpg.de/cresst/NIM2000.zip>).
- [8] J.D. Lewin and P.F. Smith, Astropart. Phys. **6** (1996) 87.
- [9] G. Jungman, M. Kamionkowski and K. Griest, Phys. Rep. **267** (1996) 195.
- [10] R.H. Helm, Phys. Rev. 104 (1956) 1466.
- [11] J. Engel et al., Phys. Rev **C 52** (1995) 2216.
- [12] A. Allesandrello et al., Phys. Lett. **B 384** (1996) 316.
- [13] L. Baudis et al., Phys. Rev. **D 59** (1999) 022001.
- [14] S. Cebrian et al. Astropart. Phys. **15** (2001) 79.
- [15] D.R. Tovey et al., Phys. Lett. **B 488** (2000) 17
- [16] A. de Bellefon et al., Astroparticle Physics 6 (1996) 35.
- [17] R. Bernabai et al., Phys. Lett. B 389 (1996) 757.
- [18] N. Spooner et al., Phys. Lett. B 473 (2000) 330.
- [19] R. Abusaidi et al., Phys. Rev. Lett. 84 (2000) 5699.
- [20] A. Benoit et al., astrp-ph/0106094 6 Jun 2001.
- [21] P. Meunier et al., Appl. Phys. Lett. 75 (1999) 1335.
- [22] R.J. Gaitskell, P.D. Barnes, A. DaSilva, B. Sadoulet, T. Shutt, Nucl. Phys. (Proc. Suppl.), 51 B (1996) 279.
- [23] L. Baudis et al., Phys. Rep. 307 (1998) 301.
- [24] R. Bernabei et al., Phys. Lett. B 450 (1999) 448.
- [25] R. Bernabei et al., Phys. Lett. B 480 (2000) 23.
- [26] R. Schnee, released TAUP Sept 1999 Conference.
- [27] V. Bednyakov, H.V. Klapdor-Kleingrothaus, S. Kovalenko, Y. Ramachers, Z. Phys. A 357 (1997) 339.